Journal of
Synchrotron
Radiation

ISSN 0909-0495

Received 29 July 2011
Accepted 19 September 2011

Probing Ag nanoparticle surface oxidation in contact with (in)organics: an X-ray scattering and fluorescence yield approach

Clement Levard,[a,b]* F. Marc Michel,[a,c] Yingge Wang,[a] Yongseong Choi,[d] Peter Eng[d] and Gordon E. Brown Jr[a,b,c]

[a]Surface and Aqueous Geochemistry Group, Department of Geological and Environmental Sciences, Stanford University, Stanford, CA 94305, USA, [b]Center for Environmental Implications of NanoTechnology (CEINT), Duke University, PO Box 90287, Durham, NC 27708-0287, USA, [c]Stanford Synchrotron Radiation Lightsource, SLAC National Accelerator Laboratory, 2575 Sand Hill Road, Menlo Park, CA 94025, USA, and [d]Consortium for Advanced Radiation Sources, University of Chicago, Chicago, IL 60637, USA. E-mail: clevard@stanford.edu

Characterizing interfacial reactions is a crucial part of understanding the behavior of nanoparticles in nature and for unlocking their functional potential. Here, an advanced nanostructure characterization approach to study the corrosion processes of silver nanoparticles (Ag-Nps), currently the most highly produced nanoparticle for nanotechnology, is presented. Corrosion of Ag-Nps under aqueous conditions, in particular in the presence of organic matter and halide species common to many natural environments, is of particular importance because the release of toxic Ag^+ from oxidation/dissolution of Ag-Nps may strongly impact ecosystems. In this context, Ag-Nps capped with polyvinolpyrrolidone (PVP) in contact with a simple proxy of organic matter in natural waters [polyacrylic acid (PAA) and Cl^- in solution] has been investigated. A combination of synchrotron-based X-ray standing-wave fluorescence yield- and X-ray diffraction-based experiments on a sample consisting of an approximately single-particle layer of Ag-Nps deposited on a silicon substrate and coated by a thin film of PAA containing Cl revealed the formation of a stable AgCl corrosion product despite the presence of potential surface stabilizers (PVP and PAA). Diffusion and precipitation processes at the Ag-Nps–PAA interface were characterized with a high spatial resolution using this new approach.

Keywords: silver nanoparticles; environmental interfaces; corrosion processes; thin films.

1. Introduction

Reactions occurring at the solid–water interface of nanosized particles, both natural and synthetic, are of increasing scientific and technological interest owing to their impacts on (geo)chemical systems. In this context, nanoparticles are of a particular interest since a relatively high percentage of the atoms that constitute the particle are located at the surface. In the environment, interfacial reactions involving naturally occurring nanoparticles are known to play a significant role in the speciation, transformation and sequestration of a wide variety of pollutants (*e.g.* Levard *et al.*, 2009). Manufactured nanoparticles are exploited for their enhanced reactivity and catalytic behavior, along with other physical and chemical properties. Industrial-scale manufacturing of nanoparticles for use in nanotechnology, as well as in catalysis and electronics, is projected to increase (Blaser *et al.*, 2008). In turn, the amount of manufactured nanoparticles released to the environment through waste streams is also likely to increase and there is concern that their enhanced reactivity may negatively impact biota, as well as soil and water quality (Marambio-Jones & Hoek, 2010; Khaydarov *et al.*, 2009). A deeper understanding of the fundamental processes associated with nanoparticle reactivity is therefore needed to evaluate their environmental impact, as well as to unlock their functional potential.

Interfacial reactions such as dissolution (either oxidative or reductive), precipitation and sorption occurring for bulk materials have been studied for decades using a variety of scattering and spectroscopic approaches. Methods such as X-ray diffraction, X-ray absorption and emission spectroscopies, to name just a few, provide powerful means for obtaining phase and/or chemical information with high resolution and sensitivity. However, with decreasing particle size, in particular for sizes less than a few tens of nanometers, the

information obtainable by these methods generally becomes less spatially resolved because the samples can usually only be measured in a polycrystalline form rather than as oriented single crystals, for example. In the case of nanoparticles in contact with natural matrices, additional challenges can arise owing to the complexity of phases such as natural organic matter (NOM).

Our approach in this study builds on past experiments involving multi-layered samples composed of oriented and polished single crystals of metal oxides that were coated with organic matter in the form of microbial biofilms (Trainor *et al.*, 2002; Templeton *et al.*, 2001, 2003, 2005). These studies explored the chemical partitioning of selected elements between two pools of reactive sites; those occurring on specific facets of the metal oxide surface and those of the functional groups present in the overlying organic matter. Here, we are expanding the utility of this approach by applying it to a multi-layered sample composed of a thin film of nanosized silver particles (Ag-Nps) supported on a silicon wafer substrate and coated with a polyacrylic acid (PAA) solution. PAA served as a simplified analogue of NOM such as humic substances, which is known to be a reactive component in natural systems in part due to a variety of functional groups, such as carboxyl, that complex with minerals, metal and metalloid species (Roger *et al.*, 2010; Floroiu *et al.*, 2001). Our goal was to test a novel approach for characterizing a reaction between the Ag-Nps, which were capped with polyvinylpyrrolidone (PVP), and the PAA which contained chloride and bromide in solution. We applied a combination of long-period X-ray standing-wave fluorescence-yield (XSW-FY) spectroscopy, grazing-incidence X-ray diffraction (GI-XRD) and long-period XSW-based X-ray diffraction (XSW-XRD) to obtain chemical- and phase-specific information. This approach generated a picture of the multi-layer system that is highly spatially resolved (nanometer range) and that contains both phase and chemical information regarding the reactants and products. To the best of our knowledge, this combination of techniques has never been applied to characterize the reaction of nanoparticles in contact with an aqueous solution.

Silver was chosen as the focus for this study because of recent interest in understanding the dissolution of Ag-Nps, as well as the diffusion, precipitation and transformation of their released species, some of which are potentially toxic (Marambio-Jones & Hoek, 2010). Ag-Nps are the most widely used in nanotechnology mainly because of their antimicrobial and antifungal properties (Rejeski *et al.*, 2010). By assessing the stability of the PVP-capped Ag-Nps with average sizes of 20 ± 4 nm in the presence of potential surface stabilizers (PVP and PAA) and a potential surface oxidant (Cl^-), our main goal was to demonstrate that the proposed approach, usually dedicated to the characterization of oriented surfaces, can be successfully applied to study the reactivity of nanoparticles in contact with a complex system. We believe this general approach is well suited for studying a variety of multi-layered systems with nano-sized dimensions, including *in situ* kinetic studies of dissolution/precipitation.

In addition to demonstrating the proposed technique, our results also begin to explore the effects of adsorbed organic ligands at Ag-Nps surfaces on modifying their stability, reactivity and solubility by promoting or inhibiting corrosion. The association of Ag-Nps with NOM is expected owing to the ubiquity of NOM in ecosystems. In industry, organics such as citrate or PVP are commonly used as a nanoparticle surface capping agent during manufacturing to control particle size and aggregation through surface passivation (Tolaymat *et al.*, 2010). Also, NOM such as humic substances can mitigate short-term bacterial toxicity of citrate-coated Ag-Nps (Fabrega *et al.*, 2009). Humic substances, which likely form films on Ag-Nps surfaces, should reduce their dissolution rate by surface passivation (Fabrega *et al.*, 2009). However, the corrosive effects of common aqueous anions, such as Cl^-, which react strongly with clean Ag-Nps surfaces (Jones, 1988; Graedel, 1992; Andryushechkin *et al.*, 2007), are not well understood in the case of nanoparticles in the presence of organic coatings.

2. Materials and methods

2.1. Materials

The 20 ± 4 nm quasi-spherical PVP-capped Ag-Nps have been synthesized following a protocol adapted from Kim *et al.* (2006). First, PVP (M_w = 10000, m = 15 g) was dissolved in 50 ml of ethylene glycol. The solution was then heated to 393 K. Silver nitrate ($AgNO_3$) was dissolved in deionized water (825 mg, 40 wt%) and injected into the ethylene glycol solution at the reaction temperature. The reaction time was set at 2 h. Once the solution cooled to room temperature, the silver nanoparticles were separated with acetone and then centrifuged. Finally, the Ag-Nps were washed twice with deionized water, centrifuged and redispersed in ethanol (final concentration: 4 g L^{-1}). The Ag-Nps were washed again with ethanol immediately before being deposited on a silicon wafer substrate *via* spin-coating (6000 r.p.m., 20 s). The second ethanol wash was to remove excess PVP and Ag^+ that might have desorbed during storage. The final PVP-capped Ag-Nps film was heated at 373 K for 30 min to improve the adhesion between the Ag-Nps and the silicon wafer. A 2% solution of PAA (pH = 6.5; 0.01 mol L^{-1} $NaNO_3$) with initial Cl and Br concentrations of 0.014 mol L^{-1} and 1.25×10^{-4} mol L^{-1}, respectively, was applied to the Si-wafer-supported Ag-Nps thin film layer and aged during 24 h (Fig. 1*a*). After 24 h of reaction time the PAA was spin-coated leading to a dry multi-layered sample (Si-wafer/PVP-capped Ag-Nps/PAA). The characterization data presented in this paper were obtained on the final dried sample.

2.2. Methods

Synchrotron-based characterizations were performed at beamline 13-ID-C of the Advanced Photon Source. The general experimental set-up for X-ray characterization is shown in Fig. 1(*b*) and was used for four types of synchrotron-based measurements: (i) specular reflectivity to characterize

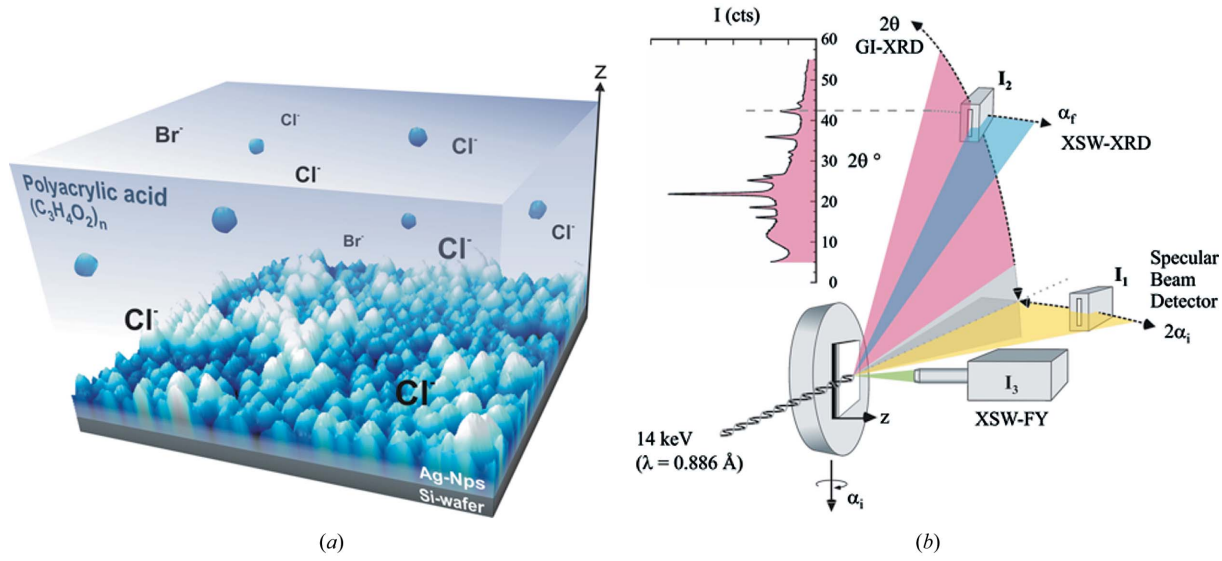

(*a*) (*b*)

Figure 1
Conceptual figures of the sample and experimental set-up. (*a*) The sample studied was formed from a PAA solution applied to and aged on a thin film of PVP-capped Ag-Nps initially deposited on a Si-wafer support (actual AFM image of Ag-Nps shown). The Ag-Nps (blue spheres) shown suspended in the PAA represent a small fraction of Ag-Nps that detached from the substrate during aging. (*b*) Experimental set-up for the fluorescence yield and diffraction-based measurements as well as specular reflectivity using 14 keV synchrotron X-rays. The reflectivity was measured as a function of α_i and $2\alpha_i$ (°) using an ion chamber (I_1); the grazing-incidence XRD and XRD-based X-ray standing-wave profiles (XSW-XRD) were measured as a function of 2θ (°) and α_f (°), respectively, using a two-dimensional array detector (I_2). Fluorescence yield was measured orthogonal to the sample using a high-resolution fluorescence detector (I_3).

the vertical density profile of the sample as well as film thickness and interface roughness [Fig. 1(*b*), yellow arc]; (ii) long-period XSW-FY intensity measurements as a function of incidence angle (α_i) to the sample in order to obtain the vertical chemical distribution of Ag and species initially present in the PAA (*e.g.* Cl, Br) between the Ag-Nps layer and overlying PAA film [Fig. 1(*b*), green]; (iii) grazing-incidence (GI)-XRD to characterize the primary (metallic Ag, Ag^0) and secondary crystalline phases formed during aging, if present [Fig. 1(*b*), pink arc]; and (iv) XSW-XRD profiles as a function of α_i [Fig. 1(*b*), blue arc] to characterize the vertical distribution of different crystalline phases between the Ag-Nps layer and overlying PAA film.

In measuring synchrotron-based specular reflectivity, the angle between the incident X-rays and the sample is scanned by varying the angle of the sample α_i (0–0.5°) while the intensity of the specularly reflected X-rays is detected at an angle $2\alpha_i$ (0–1.0°) from the incident beam. X-ray specular reflectivity was fitted using a routine based on Parratt's recursion formula (Parratt, 1954) and a model consisting of a relatively low density layer, representing PAA, and a high-density layer, representing PVP-capped Ag-Nps. Fitted parameters include the density and thickness of each layer as well as the roughness of the different interfaces. The resulting fit parameters are used to calculate the electric field intensity profile described below.

Fluorescence yield and synchrotron-based X-ray standing waves are generated by the superposition of coherently coupled incident and reflected X-ray beams, leading to an enhancement of both the fluorescence and diffraction signals, which are highly sensitive to vertical variations in composition and phase type. The constructive interference of the incident and reflected beams create the antinodes of the XSW, and the number and positions of the antinodes relative to the reflecting substrate can be varied, in this case by changing the angle of incidence α_i. As such, the probing depth (z) is controllable. At incidence angles well below the critical angle of the Ag-Nps film, the antinodes of the XSW are positioned in the PAA film primarily, whereas, at higher angles near the critical angle of the Ag-Nps layer, some of the antinodes are positioned near the substrate (*i.e.* at the PVP-capped Ag-Nps film, see Fig. S1 of the supplementary information[1]). The fluorescence yield (FY) for the elements of interest in the system is monitored during this process and as a function of incident X-ray angle using a Vortex four-element silicon drift detector. Each spectrum shown in Fig. 4(*a*) is an average of the four channels of the Vortex detector before background-subtraction, correction for attenuation from the sample-to-detector path length (He), filters (*e.g.* Kapton film), or the net FY of each element. Figs. 4(*b*)–4(*d*) include background subtraction and these corrections.

The XSW-FY data can be fitted using a general scattering model, which allows quantification of the vertical distribution of specific elements. The FY data were subsequently modeled using equation (1) (Bommarito *et al.*, 1990; Bedzyk *et al.*, 1990; Abruña *et al.*, 1990),

$$\mathrm{FY}(\alpha_i) = \int I(z, \alpha_i) N(z) \exp[-(z/L_a)]\, \mathrm{d}z, \qquad (1)$$

where $N(z)$ is the depth profile of the fluorescing element, L_a is the attenuation length of the outgoing fluorescence, and

[1] Supplementary data for this paper are available from the IUCr electronic archives (Reference: HF5193). Services for accessing these data are described at the back of the journal.

$I(z,\theta)$ is the electric field intensity at depth z and angle θ. The complete electric field intensity profile $I(z,\theta)$ above and below the surface is calculated using Parratt's recursive formalism with the parameters obtained from the reflectivity fits (Parratt, 1954; Krol *et al.*, 1988; Deboer, 1991).

Attenuation of the emitted fluorescence intensity owing to the sample-to-detector path length (He filled) and filters (kapton) is accounted for in the calculation. The elemental distribution was modeled using a two-box model similar to previous studies (Yoon *et al.*, 2005; Templeton *et al.*, 2001). In our case the film layer can be divided into two regions: (i) near the Si-wafer surface that includes the sum of the PVP-capped Ag-Nps layer thickness (115 Å) and the Ag-Nps/PAA interface roughness (38 Å), and (ii) the remaining thickness of the PAA film (770 Å). A least-squares fitting routine written in *Igor Pro* was used to fit individual scaling factors for each region of the two-box distribution model, from which the calculated elemental partitioning profiles are obtained [Figs. 4(*b*)–4(*d*)].

In measuring GI-XRD, the scattering intensity is detected using a Dectris Pilatus 100k pixel array detector for 2θ angles ranging from 5 to 55°. GI-XRD profiles were collected with the incident X-rays fixed at seven discrete angles relative to the sample (Fig. 4*b*). GI-XRD data are analyzed by fitting with known structural models (ICSD numbers for Ag^0, AgCl) using the Rietveld method in order to obtain lattice parameters and relative abundance of the crystalline phases present. In measuring XSW-XRD, the intensity of selected diffraction peaks (*i.e.* fixed angle 2θ) were measured as the angle between the incident X-rays and the sample is scanned by varying the angle of the sample (α_i, 0–0.5°). The XSW-XRD data can be fitted using the same formalism as presented in equation (1) which allows quantification of the vertical distribution of specific phases. In this case the attenuation can be ignored owing to the high energy of the reflected beam.

Auger spectroscopy, scanning electron microscopy (SEM) and atomic force microscopy (AFM) were used for local-scale characterization. The thicknesses and physical aspects of individual films were obtained from SEM images collected with a FEI XL30 Sirion SEM (accelerating voltage, 5 kV) with a tilt of 45° [Figs. 3(*b*)–3(*d*)] or without [Figs. 3(*a*)–3(*c*)]. SEM samples were coated with gold prior to the experiment to avoid charging effects owing to the PVP/PAA. AFM images were obtained using a Park Systems XE-70 model scanning probe microscope in a non-contact mode. AFM raw data were processed with the XEI commercial software.

3. Results and discussion

3.1. Film properties

The thickness and density of each layer in the multi-layer film varies with composition, and the three resulting interfaces (*i.e.* air/PAA, PAA/Ag-Nps, Ag-Nps/Si-wafer) vary in roughness. The X-ray reflectivity profile was fit using a multi-layer model composed of Si-wafer, PVP-coated Ag-Nps and PAA (Fig. 2). All parameters were refined simultaneously using

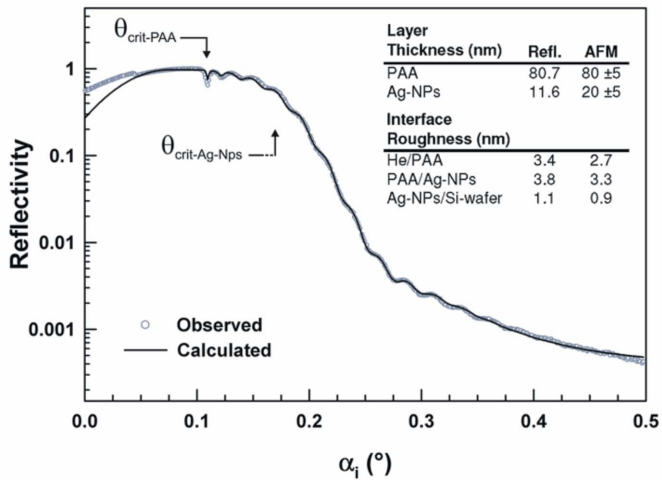

Figure 2
Specular reflectivity fitting and AFM results. The measured reflectivity profile (open symbols) was fitted using a multi-layer model composed of Si-wafer, Ag and PAA (black solid line). The approximate critical angles of both the PAA and the PVP-capped Ag-Nps thin films are shown as $\theta_{crit\text{-}PAA}$ and $\theta_{crit\text{-}Ag\text{-}Nps}$, respectively. The table includes the thickness and interface roughness values from reflectivity fitting and AFM measurements.

reasonable starting values. Although the average diameter of the PVP-capped Ag-Nps from SEM is 20 ± 4 nm, the thickness of the Ag-Nps film from fitting the X-ray reflectivity data is lower than expected (11.6 ± 0.2 nm). Similarly, the density of Ag-Nps film (5.8 g cm^{-3}) from fitting is lower than expected for bulk silver (10.4 g cm^{-3}), and the deviation is likely to be due to the presence of PVP and spaces filled with PAA and/or air between individual nanoparticles. What is effectively measured from specular reflectivity is a laterally averaged electron density profile. The measurement is sensitive to the change in the film depth direction (z), and the measured signal contains an averaged signal from all of the illuminated area. Thus, the shape of the nanoparticles and voids present in between adjacent particles (Fig. 3*b*) explain both the lower thickness and density obtained from the reflectivity refinement. Except for these two parameters for the PVP-coated Ag-Nps layer, film properties obtained from the fitting of the X-ray reflectivity profile are in agreement with direct physical measurements (AFM and SEM) (see table in Fig. 2, and Fig. 3).

The PAA film thickness deduced from the X-ray reflectivity profile (80.7 ± 0.5 nm) is consistent with the value obtained from AFM measurement (80–85 nm). Finally, the roughness values for the PAA/air interface (3.4 ± 0.03 nm), Ag-Nps/PAA interface (3.8 ± 0.01 nm) and Si-wafer/Ag-Nps interface (1.1 ± 0.01 nm) obtained from the X-ray reflectivity data are the same order of magnitude as that measured by AFM (∼2.7, ∼3.8 and ∼0.9 nm, respectively).

SEM and AFM images (Fig. 3 and Fig. S2) also reveal features at the PAA/air interface that are not apparent from the X-ray reflectivity data. The sample aged for 24 h has relatively large particles up to 250 nm in diameter associated with the PAA film. These large particles were not present initially in the PVP-capped Ag-Nps film or PAA solution and

resulted from the reaction of the PVP-capped Ag-Nps and the PAA solution.

3.2. Vertical elemental distribution

FY intensities collected at energies ranging from ~2 to ~14 keV (Fig. 4*a*) and different X-ray incidence angles reveal the distribution of elements in this multi-layer system, which includes Si, Cl, Br and Ag. Cl and Br were not added to the sample but were present in the initial PAA solution. The XSW-FY profiles for Ag, Cl and Br absorption edges collected at α_i angles ranging from 0 to 0.5° are presented in Figs. 4(*b*), 4(*c*) and 4(*d*). Peaks in the FY profile (Fig. 4*b*, peaks #1–7) correspond to increases in the electric field intensity owing to constructive interference of the incident and reflected X-ray beams (see §2.2).

Fitting the FY profiles using a two-box model indicates that the highest concentration of Ag (90.3%) (Table 1) is in the PVP-capped Ag-Nps layer. The remaining 9.7% of Ag occurs in the PAA film and may correspond to both suspended PVP-capped Ag-Nps that have migrated into the PAA film and dissolved Ag^+ that has diffused into the PAA film after dissolution from the Ag-Nps. Both Cl and Br are mainly observed in the Ag-Nps film (87% and 94.4%, respectively). Both Cl and Br exhibit a strong affinity for Ag (Wiley *et al.*, 2004; Cathcart *et al.*, 2009; An *et al.*, 2008), and their association at ambient temperature and pressure results in the formation of relatively insoluble Ag*X* complexes (where *X* = Br^- and Cl^-, $-\log K_{sp}$ = 12.27 and 9.75 for AgBr and AgCl, respectively) (Lide, 2009). However, it is unclear from the FY intensities alone whether Br and Cl are associated with the PAA and/or PVP or with silver in the form of sorbed complexes or surface precipitates and/or as separate crystalline AgBr or AgCl phases. The latter is suggested by the presence of the relatively large particles in the 24 h sample [Fig. 3(*c*) and Fig. S2].

Table 1
Distribution of selected elements and crystalline phases in the PAA film and in the PVP-capped Ag-Nps film.

Elemental distributions

	PAA film (%)	Ag-Nps film (%)
Ag	9.7	90.3
Br	5.4	94.6
Cl	13.4	86.6
Ag:Cl	3.6	5.2
Ag:Br	442.3	235
Cl:Br	122.3	45.1

Phase distributions

	PAA film (%)	Ag-Nps film (%)
$AgCl_{(s)}$	51	49
$Ag^0_{(s)}$	8	92

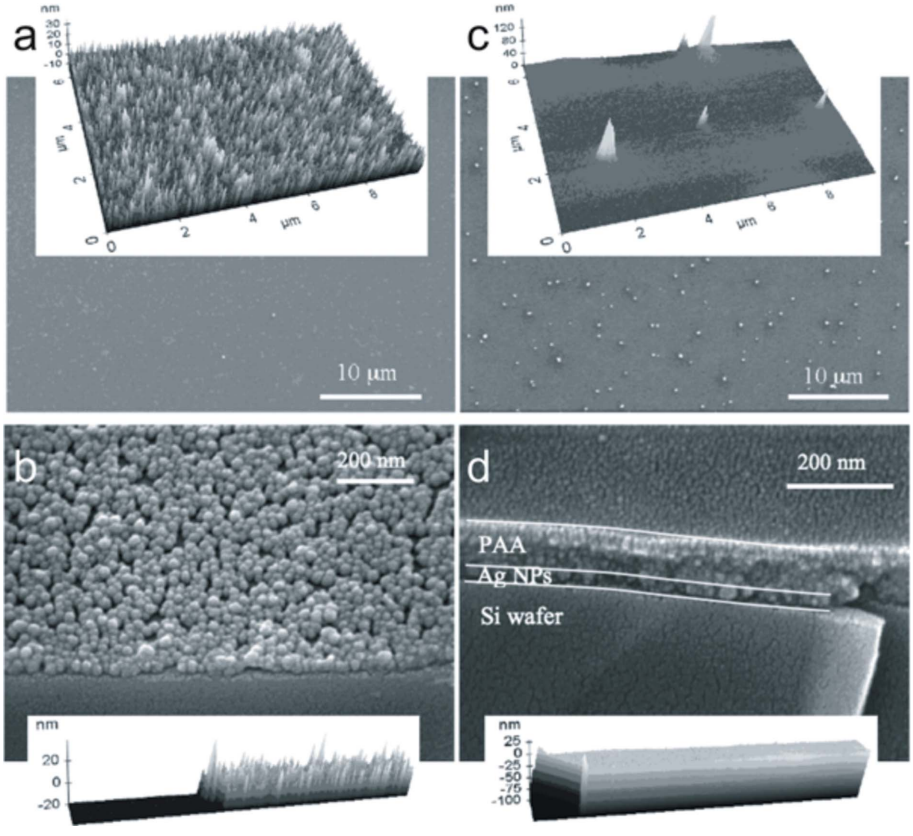

Figure 3
Imaging of Ag-Nps thin film with and without PAA coating. (*a*, *b*) SEM and AFM (overlays) images of the PVP-capped Ag-Nps film uncoated and (*c*, *d*) coated with PAA.

3.3. Solid phase identification and vertical distribution

Analysis of GI-XRD data [Fig. 1(*b*), pink arc] collected at selected incidence angles α_i complements the chemical information from the XSW-FY measurements by providing additional information on solid phases as well as the spatial association of different crystalline solids that may have formed. At high incidence angle [Fig. 5(*b*), α_i #7], above the critical angles of both PAA and Ag, the five major peaks observed in the diffraction data correspond to the known structure of metallic Ag [Fig. 5(*a*), scan #7]. Additional minor features suggest the presence of a second phase. At relatively low incidence angles [Fig. 5(*b*), α_i #1], slightly above the critical angle of PAA but below that of the Ag-Nps, the diffracted intensity profile is primarily representative of the PAA film. At this angle of incidence [Fig. 5(*a*), scan #1] it is clear that the PAA film contains two crystalline phases consistent with the known structures of metallic Ag and

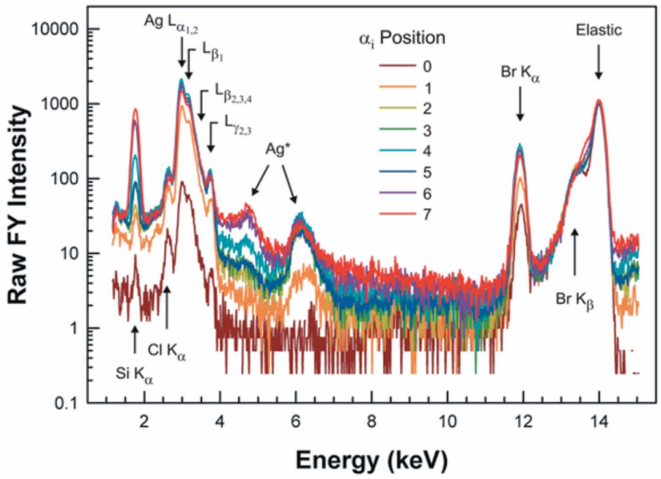

(*a*)

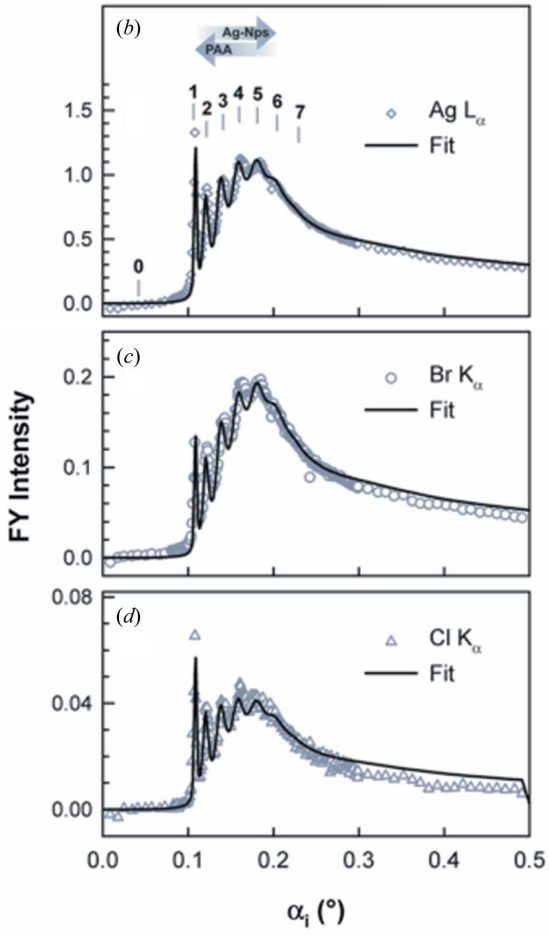

Figure 4
Total emission spectra and element-specific XSW-FY profiles. (*a*) Total X-ray emission spectra collected at eight selected α_i angles 0–7 in (*b*). The signal from Si is primarily from the substrate, although additional impurities, *e.g.* Cl and Br, are also present in the initial PAA solution. The elastic peak corresponds to the incident X-ray energy (14 keV) and Ag* is attributed to pulse processor pile-up owing to the high count rate for the Ag *L*-edge emission lines. (*b*, *c*, *d*) Measured XSW-FY intensities for Ag, Cr and Cl (open symbols). Fine-structure oscillations (1–7) in the XSW profiles are the result of interference between incoming and outgoing X-rays from the different interfaces in the multi-layered sample (see additional details in §2.2).

AgCl. Auger analysis of the larger particles observed by SEM/AFM confirms that the main elemental constituents are Cl, Ag and C with an Ag/Cl ratio of 1.7 (Figs. S3 and S4). The amount of Cl relative to Ag decreased with the number of scans for the same analysis area and can be explained by electron-beam stimulated desorption of Cl during repeated scans on the particle (Behrish & Townsend, 1983). In contrast, only Ag and C (from the PAA) were detected in an area of the sample with no apparent particles (Fig. S3). In this case the signal from Ag is possibly from Ag nanoparticles that have detached from the PVP-capped Ag-Nps layer and moved into the PAA layer and/or from dissolved Ag. These observations suggest that AgCl precipitated owing to the reaction of dissolved Ag^+ with Cl^- present in the PAA during aging.

While useful for evaluating the elemental distribution in the multi-layer sample, the XSW-FY intensity does not reveal the vertical distribution of the different crystalline phase(s) present in each layer, particularly when the phases have similarities in chemical composition (*e.g.* Ag^0 and AgCl). However, the phase distribution of the sample can be obtained from XSW-XRD. This information is necessary for evaluating the possible migration of PVP-capped Ag-Nps into the PAA film as well as the formation and spatial distribution of new crystalline phase(s) by tracking the intensity of specific diffraction maxima (either Ag^0 or AgCl in our case) as a function of incidence angle [XRD-XSW, Fig. 1(*b*), blue arc]. As expected, the fitting of the XSW-XRD profiles suggests a strong contribution of Ag^0 (92%) in the PVP-capped Ag-Nps film and a lesser contribution in the PAA film (8%) (Table 1). In contrast, the XSW-XRD profile based on the diffraction maxima for AgCl suggests that this phase is approximately evenly distributed between the PAA film (49%) and the PVP-coated Ag-Nps film (51%). The important proportion of AgCl observed in the PAA film is consistent with the observation of new-formed particles in the PAA (Fig. 3*c*), identified as a silver chloride phase (Auger analysis, Figs. S3 and S4). The dissolved Ag and Cl species in the PAA precipitate as crystalline AgCl. This finding is consistent with a simple thermodynamic simulation that considers the concentration of Ag, Cl and carboxyl (present in the PAA) in the system (Fig. S5). Under these conditions, complexation of Ag with the carboxylic group seems unlikely considering the strong affinity of Ag for Cl.

The formation of AgCl during aging of the PVP-capped Ag-Nps thin film implies the following steps occurred: (i) Ag is oxidized, presumably at Ag-Nps surfaces, (ii) oxidized and soluble aqueous Ag^+ species diffuse into the PAA solution, (iii) Ag^+ reacts with chloride ions initially present in the PAA solution resulting in the formation of the stable AgCl complex, and (iv) the PAA solution becomes saturated with respect to $AgCl_{(s)}$ and precipitation of $AgCl_{(s)}$ occurs. Analysis of the XSW-FY data reveals that Br is present in the PAA solution, and this species would also be expected to react with dissolved Ag^+. However, based on the concentrations extracted from the XSW-FY intensities (Fig. 4), Br is 122.3 and 45.1 times less abundant than Cl in the PAA film and in the Ag-Nps film, respectively (Table 1). Although $AgBr_{(s)}$ was not detected by

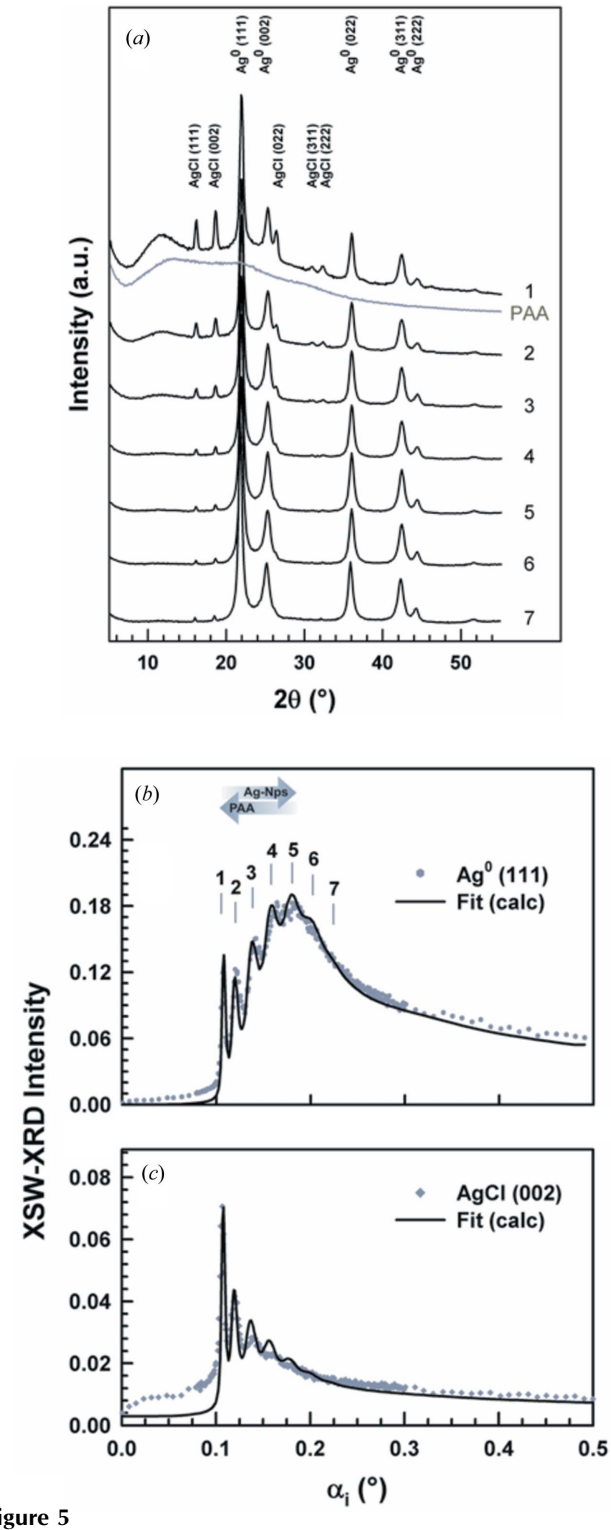

Figure 5
GI-XRD and XRD-based XSW for AgCl and Ag^0. (*a*) GI-XRD profiles collected at the seven incidence (α_i) angles shown in (*b*). Diffraction maxima from crystalline phases can be indexed with the known structures of AgCl and metallic Ag. Diffuse scattering from an unreacted PAA is shown for comparison (solid grey). (*b*, *c*) XRD-based X-ray standing waves from diffraction features corresponding to Ag-Nps (Ag^0) or AgCl. The Ag^0 and AgCl profiles were obtained from tracking the intensities of the (111) and (002) reflections, respectively, as a function of incidence angle (α_i). The individual XRD-based standing-wave profiles were each fitted with the same two-box model used for the XSW-FY data shown in Fig. 4.

XRD, AgBr complexes and/or precipitates may be present in the PAA film in minor abundance. Interestingly, the XSW-FY profiles for Br and Cl both show that these elements preferentially partition to the PVP-coated Ag-Nps thin film. As shown in Table 1, 5.4% and 13.4% of the total Br and Cl, respectively, partition to the PAA film, with the remainder of each in the Ag-Nps film. The relatively high percentage of Cl in the Ag-Nps film obtained from the fitting of the XSW-FY profile (86.6%) compared with the amount of AgCl obtained from fitting the XSW-XRD profile (49%) suggests the presence of amorphous AgCl, not detected by XRD-based techniques associated with the PVP-capped Ag-Nps more likely as surface precipitates. Similarly, the high proportions of Br in the Ag-Nps film and apparent lack of crystalline $AgBr_{(s)}$ phases associated with the Ag-Nps film suggest the presence of AgBr surface precipitates which are most likely amorphous.

The strong partitioning of Cl and Br in the Ag-Nps film suggests that these elements may actively participate in the oxidation of the Ag-Nps. Wiley and co-workers report that the presence of Cl combined with oxygen results in the enhanced oxidation and preferential etching of Ag-Nps (Wiley *et al.*, 2004). Also, Br has been shown to react similarly to Cl with respect to Ag-Nps (Cathcart *et al.*, 2009). The dissolution of Ag-Nps and re-precipitation of $AgCl_{(s)}$ in 24 h under the conditions of our experiments suggests that the kinetics of these processes are relatively fast and that the presence of organics (PVP and PAA) do not prevent surface corrosion.

Our findings suggest a three-step process in the interaction of PAA and dissolved halogens with the PVP-capped Ag-Nps layer: (i) PVP-coated Ag-Nps are partially oxidized in the presence of the PAA and halogens during aging; (ii) dissolution of PVP-coated Ag-Nps results in the diffusion of dissolved Ag^+ species into the PAA film; and (iii) dissolved Ag^+ species co-precipitate with Cl^- within the PAA film forming $AgCl_{(s)}$. Cl and Br are closely associated with the Ag-Nps surfaces, as shown by the XSW-FY profiles, and thus may increase the dissolution rate of the Ag-Nps through a corrosion process, as has been shown for Cl^- in an earlier study of uncoated Ag thin films (Bilmes, 1996). The impact of PAA and PVP on this process is not clear but may slow down the kinetics of corrosion by passivating the surface. Further experiments using the same set-up on uncoated Ag-Nps are currently underway to test this hypothesis. Furthermore, the reaction of dissolved Ag^+ species, for example with halogens, is also of importance since the formation of secondary precipitates (*e.g.* AgCl, AgBr) may effectively sequester toxic Ag^+ in a solid form that is relatively inert and stable. Considering the high abundance of chloride in natural systems, it is reasonable to expect that the toxicity of Ag-Nps owing to the release of dissolved Ag^+ species will be reduced as a result of these precipitation processes.

3.4. Implication of this work

This study offers a new approach for investigating the reactivity of nanoparticles in contact with (in)organic compounds and opens new opportunities to understand the

kinetics and the role of organics on the corrosion of Ag-Nps. Future work using this approach will explore the stability of Ag-Nps under reducing conditions to determine the role of oxygen on the kinetics of corrosion processes. The example presented in this study demonstrates the complementary nature of XSW-FY, GI-XRD and XSW-XRD techniques for obtaining both compositional and crystalline phase distribution information with good spatial resolution on a multilayered system. Such an approach provides new insights about complex chemical processes involving nanoparticles in natural systems and could also be used in studies of a variety of multilayered systems with nanosized dimensions, including *in situ* kinetic studies of dissolution/precipitation.

This material is based upon work supported by the National Science Foundation (NSF) and the Environmental Protection Agency (EPA) under NSF Cooperative Agreement EF-0830093, Center for the Environmental Implications of NanoTechnology (CEINT). Any opinions, findings, conclusions or recommendations expressed in this material are those of the author(s) and do not necessarily reflect the views of the NSF or the EPA. This work has not been subjected to EPA review and no official endorsement should be inferred. Use of the Advanced Photon Source, an Office of Science User Facility operated for the US Department of Energy (DOE) Office of Science by Argonne National Laboratory, was supported by the US DOE under Contract No. DE-AC02-06CH11357.

References

Abruña, H. D., Bommarito, G. M. & Acevedo, D. (1990). *Science*, **250**, 69–74.
An, J., Tang, B., Zheng, X. L., Zhou, J., Dong, F. X., Xu, S. P., Wang, Y., Zhao, B. & Xu, W. Q. (2008). *J. Phys. Chem. C*, **112**, 15176–15182.
Andryushechkin, B. V., Eltsov, K. N. & Shevlyuga, V. M. (2007). *Phys. Wave Phenom.* **15**, 116–125.
Bedzyk, M. J., Bommarito, G. M., Caffrey, M. & Penner, T. L. (1990). *Science*, **248**, 52–56.
Behrish, R. & Townsend, P. (1983). *Topics in Applied Physics*, Vol. 52, *Sputtering by Particle Bombardment II*, pp. 147–178. Berlin: Springer.
Bilmes, S. A. (1996). *J. Chem. Soc. Faraday Trans.* **92**, 2381–2387.
Blaser, S. A., Scheringer, M., Macleod, M. & Hungerbühler, K. (2008). *Sci. Total Environ.* **390**, 396–409.
Bommarito, G. M., White, J. H. & Abruna, H. D. (1990). *J. Phys. Chem.* **94**, 8280–8288.
Cathcart, N., Frank, A. J. & Kitaev, V. (2009). *Chem. Commun.* pp. 7170–7172.
Deboer, D. K. G. (1991). *Phys. Rev. B*, **44**, 498–511.
Fabrega, J., Fawcett, S. R., Renshaw, J. C. & Lead, J. R. (2009). *Environ. Sci. Technol.* **43**, 7285–7290.
Floroiu, R. M., Davis, A. P. & Torrents, A. (2001). *Environ. Sci. Technol.* **35**, 348–353.
Graedel, T. E. (1992). *J. Electrochem. Soc.* **139**, 1963–1970.
Jones, R. G. (1988). *Prog. Surf. Sci.* **27**, 25–160.
Khaydarov, R. R., Khaydarov, R. A., Estrin, Y., Evgrafova, S., Scheper, T., Endres, C. & Cho, S. Y. (2009). *Nanomaterials: Risks and Benefits*, pp. 287–297. Dordrecht: Springer.
Kim, D., Jeong, S. & Moon, J. (2006). *Nanotechnology*, **17**, 4019–4024.
Krol, A., Sher, C. J. & Kao, Y. H. (1988). *Phys. Rev. B*, **38**, 8579–8592.
Levard, C., Doelsch, E., Rose, J., Masion, A., Basile-Doelsch, I., Proux, O., Hazemann, J. L., Borschneck, D. & Bottero, J. Y. (2009). *Geochim. Cosmochim. Acta*, **73**, 4750–4760.
Lide, D. R. (2009). *Handbook of Chemistry and Physics.* Boca Raton: CRC Press.
Marambio-Jones, C. & Hoek, E. M. V. (2010). *J. Nanopart. Res.* **12**, 1531–1551.
Parratt, L. G. (1954). *Phys. Rev.* **95**, 359–369.
Rejeski, D., Kulken, T., Pollschuk, P. & Pauwels, E. (2010). *The Project on Emerging Nanotechnologies*, http://www.nanotechproject.org/inventories/consumer/analysis_draft/.
Roger, G. M., Durand-Vidal, S., Bernard, O., Meriguet, G., Altmann, S. & Turq, P. (2010). *Colloids Surfaces A*, **356**, 51–57.
Templeton, A. S., Trainor, T., Brown, G. E. & Tebo, B. M. (2005). *Geochim. Cosmochim. Acta*, **69**, A613.
Templeton, A. S., Trainor, T. P., Spormann, A. M. & Brown, G. E. (2003). *Geochim. Cosmochim. Acta*, **67**, 3547–3557.
Templeton, A. S., Trainor, T. P., Traina, S. J., Spormann, A. M. & Brown, G. E. (2001). *Proc. Natl Acad. Sci. USA*, **98**, 11897–11902.
Tolaymat, T. M., El Badawy, A. M., Genaidy, A., Scheckel, K. G., Luxton, T. P. & Suidan, M. (2010). *Sci. Total Environ.* **408**, 999–1006.
Trainor, T. P., Templeton, A. S., Brown, G. E. & Parks, G. A. (2002). *Langmuir*, **18**, 5782–5791.
Wiley, B., Herricks, T., Sun, Y. G. & Xia, Y. N. (2004). *Nano Lett.* **4**, 1733–1739.
Yoon, T. H., Trainor, T. P., Eng, P. J., Bargar, J. R. & Brown, G. E. (2005). *Langmuir*, **21**, 4503–4511.